Asymmetric 3D Elastic–Plastic Strain-Modulated Electron Energy Structure in Monolayer Graphene by Laser Shocking

Maithilee Motlag, Prashant Kumar, Kevin Y. Hu, Shengyu Jin, Ji Li, Jiayi Shao, Xuan Yi, Yen-Hsiang Lin, Jenna C. Walrath, Lei Tong, Xinyu Huang, Rachel S. Goldman, Lei Ye,* and Gary J. Cheng**

Graphene has a great potential to replace silicon in prospective semiconductor industries due to its outstanding electronic and transport properties; nonetheless, its lack of energy bandgap is a substantial limitation for practical applications. To date, straining graphene to break its lattice symmetry is perhaps the most efficient approach toward realizing bandgap tunability in graphene. However, due to the weak lattice deformation induced by uniaxial or in-plane shear strain, most strained graphene studies have yielded bandgaps <1 eV. In this work, a modulated inhomogeneous local asymmetric elastic–plastic straining is reported that utilizes GPa-level laser shocking at a high strain rate ($d\varepsilon/dt$) ≈ 10^6–10^7 s^{-1}, with excellent formability, inducing tunable bandgaps in graphene of up to 2.1 eV, as determined by scanning tunneling spectroscopy. High-resolution imaging and Raman spectroscopy reveal strain-induced modifications to the atomic and electronic structure in graphene and first-principles simulations predict the measured bandgap openings. Laser shock modulation of semimetallic graphene to a semiconducting material with controllable bandgap has the potential to benefit the electronic and optoelectronic industries.

Graphene, which consists of a 2D atomic sheet of sp^2 hybridized carbon, is one of the most significant materials for future applications[1–18] due to its extremely high electronic mobility, quantum Hall effect, high thermal conductivity, flexibility, optical transparency, molecular anchoring capability, and superior mechanical strength. However, many electronic and optical characters are also in close relationship with finite bandgap for semiconductors, the lack of an energy bandgap in graphene hinders the realization of high-performance field-effect transistors (FET) and optoelectronic devices.[4,19–27] Moreover, modulation of the Fermi level of graphene over a large range is also very difficult to circumvent heterojunction energy barriers, thus further limiting the development of graphene-based electronic or optoelectronic devices. Although extrinsic approaches[19–21] to open the

M. Motlag, Dr. P. Kumar, Prof. K. Y. Hu, Dr. S. Jin, Dr. J. Li, Prof. G. J. Cheng
School of Industrial Engineering
Purdue University
West Lafayette, IN 47907, USA
E-mail: gjcheng@purdue.edu

Dr. P. Kumar, Prof. K. Y. Hu, Dr. S. Jin, Dr. J. Li, Dr. J. Shao, Prof. X. Yi, Prof. G. J. Cheng
Birck Nanotechnology Centre
Purdue University
West Lafayette, IN 47907, USA

Dr. P. Kumar
Department of Physics
Indian Institute of Technology Patna
Bihta Campus, Bihar 801106, India

Prof. K. Y. Hu
Department of Mechanical and Aerospace Engineering
University at Buffalo
240 Bell Hall, Buffalo, NY 14260-4400, USA

The ORCID identification number(s) for the author(s) of this article can be found under https://doi.org/10.1002/adma.201900597.

[+]Present address: Department of Physics, University of Maryland, College Park, MD 20742, USA

DOI: 10.1002/adma.201900597

Prof. X. Yi
School of Electrical and Computer Engineering
Purdue University
West Lafayette, IN 47907, USA

Dr. Y. H. Lin,[+] Dr. J. C. Walrath, Prof. R. S. Goldman
Department of Physics
University of Michigan
Ann Arbor, MI 48109, USA
E-mail: rsgold@umich.edu

L. Tong, X. Huang, Prof. L. Ye
School of Optical and Electronic Information
Huazhong University of Science and Technology
Wuhan 430074, China
E-mail: leiye@hust.edu.cn

Prof. R. S. Goldman
Department of Materials Science and Engineering
University of Michigan
Ann Arbor, MI 48109, USA

Prof. G. J. Cheng
School of Materials Engineering
Purdue University
West Lafayette, IN 47907, USA

bandgap and modulate the work function of graphene have been attempted, including doping,[22,23] hydrogen adsorption,[24] formation of graphene nanostructures[25,26] and multilayers, they have not yet been able to tune work function and yielded large bandgaps (always <1 eV);[27] as a result, the device performance based on graphene is still under restriction. Hence, an alternative method to modulate the electron energy structure of graphene is required to fully realize the potential of graphene in future semiconductor industry. To improve this intrinsic insufficiency of graphene, strain-engineering is an effective method to achieve bandgap opening. Based on the lattice symmetry of the wave vector at *K* point in graphene,[27,28] it has been suggested that uniaxial tensile or compressive strain perpendicular or parallel to the C—C bonds would break the lattice symmetry, thus opening a bandgap and changing the work function in graphene.[29–32] However, most strain-engineering work has only realized a small bandgap opening, without effective nanoscale bandgap control. To date, shear strain across bilayer graphene has been used to open the bandgap to 0.3–0.4 eV.[33] Based on first-principles calculations, Gui et al. and Hicks et al.,[34–36] have proposed that the simultaneous expansions of C—C rings in two perpendicular directions can result in a pseudo gap of 0.48 eV. Ariza et al.[37] have predicted that plastic deformation induced by the pentagonal and heptagonal rings associated with stacking faults and partial dislocations in graphene sheets would lead to significant bandgap opening of 0.8 eV. Moreover, it has been reported that the simultaneous strain and curvature in graphene would locally alter the energy band structure,[38–40] presumably leading to bandgaps exceeding 1 eV. Here, an optomechanical approach has been studied to achieve asymmetric inhomogeneous elastic–plastic strain in monolayer graphene to modulate its bandgap structure and Fermi-level, realizing bandgap development over 1.7–2.1 eV and a Fermi-level range of 0.6 eV, for the first time.

In this work, a high strain rate ($d\varepsilon/dt$) $\approx 10^6$ s^{-1} is performed by laser shock imprinting, which leads to excellent formability and toughening of graphene,[41,42] to realize inhomogeneous local asymmetric elastic–plastic strain in graphene. The strain is controllable by changing the incident laser power. Single-layer graphene was deformed via laser shocking onto an e-beam fabricated SiO_2 nanomold with designed geometries to open its bandgap, whose dimensions can precisely be controlled, resulting in patterned strain profile over large areas. In addition, the Kelvin probe force microscopy (KPFM) results of strained graphene showed that the work function is controllable with range to ≈0.6 eV, which is enough for energy barrier self-alignment in graphene–semiconductors based electronic and optoelectronic devices to achieve exciting performances. Scanning electron microscopy and atomic force microscopy were employed to characterize the deformed surface profile. Scanning tunneling spectroscopy was employed to evaluate the electronic bandgap of single-layer inhomogeneous straining graphene. The atomic-scale strains in the graphene were quantified using high-resolution transmission electron microscopy (TEM), and subsequently used as input into molecular dynamics (MD) simulations. Density functional theory (DFT) was used to perform band structure calculations. The large asymmetric plastic–elastic strain produced in graphene by laser-shocking-induced large graphene electronic bandgaps while also permitting tuning of other important characteristics such as the graphene work function. The tunable inhomogeneous straining by laser shock is highly promising for material engineering, electronic, and optoelectronic applications.[43–46]

The experimental setup schematic is depicted in **Figure 1**a. Graphene sheet is placed between the Si/SiO_2 mold and an aluminum film. The laser shock is performed on aluminum film and large strain is transduced to graphene layer. Several tens of gigapascals pressure shock is generated by tuning the laser power, thereby inducing 3D inhomogeneous strain in single-layer graphene; a small-scale MD simulation of strained monolayer graphene achieved by laser shock is shown in the inset. Figure 1b shows the evolution of nanoshaped graphene. An animation of the simulation process of producing strained monolayer graphene is depicted in Video S1 in the Supporting Information. Nanotrenches with controlled dimensions (width and depth) were fabricated on SiO_2 substrates by electron beam lithography (EBL) and then used as a mold for laser shock nanoimprinting. Figure 1c,d depicts typical molds with varying trench widths all on one substrate. More detailed scales of nanotrench molds are shown in Figure 1e,f. Atomic force microscopy images of nanostrained laser shock nanoimprinted graphene are shown in Figure 1g and enlarged Figure 1h images of the graphene having the same width of 400 nm and depth of 100 nm corresponding with the mold shape, illustrating that the smooth curvature of shaped atomic graphene atomic structure can precisely be defined by the mold dimension and the laser shock pressure. We have also measured Raman spectra of graphene after laser shocking, at eight selected point's locations of nanotrench and another location between the nanotrenches (Figure S1, Supporting Information). Their corresponding Raman spectra mapping is shown in Figure 1i. In our experiments, the laser shock is directly performed on an aluminum foil to induce large strain which is transferred to graphene, so laser induced defects in graphene can be ignored. The high-quality graphene and clean transfer method can also eliminate the influence of contaminations on Raman peak shifts. As a result, the Raman peak shifts can be attributed to the large strain in graphene. After laser shocking, the 2D peak (≈2680 cm^{-1}) and G peak (≈1600 cm^{-1}) both show obvious red shift from points b–h, indicating that the strain is largest at the trench edge, and then decreases from the trench edge to the center of the trench. To evaluate the crystal quality of graphene after laser shocking, the intensity ratio between D peak (≈1350 cm^{-1}) and G peak (I_D/I_G) is also calculated (Figure S1, Supporting Information). The ratios are smaller than 0.7, and the ratio is largest at the trench edge with largest strain. From the edge to the center of the trench, the ratios show a declining trend, with a minimum value close to that of unstrained chemical vapor deposition (CVD) monolayer graphene, which is in accordance with the strain distribution on graphene after laser shock.

The schematic diagram of the shaping of graphene is shown in **Figure 2**a. Scanning tunneling microscopy (STM)-based spectroscopy was carried out to evaluate the actual local bandgaps in the strained graphene sheet to validate our assumption that the local inhomogeneous strains caused by laser shock resulted in the opening of the bandgap of graphene. The local lattice strain profile as a function of position was calculated with

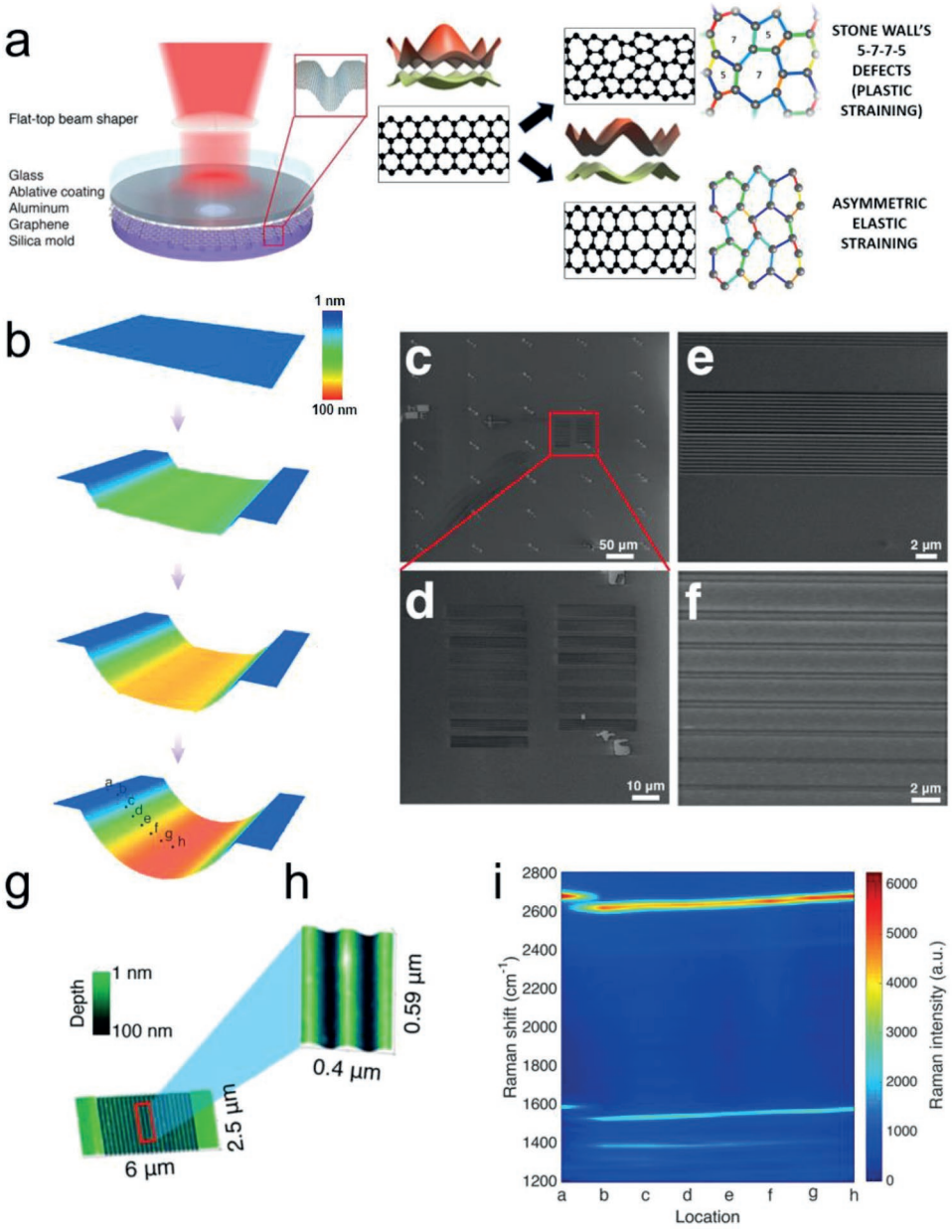

Figure 1. a) Schematic diagram illustrating experimental setup of laser shock, the inset is the depiction of nanoshaped graphene along with schematic representation of graphene's band opening due to asymmetric elastic straining and plastic straining; under elastic strain, the lattice preserves the six-atom ring structure, but under plastic strain, five and seven atom ring are emerging. b) Evolution of nanoshaped graphene under laser shock. c) FESEM image of SiO_2 mold used for the purpose; (d) and (e) show zoomed in version. f) Nanotrenches with depth 100 nm. g) AFM images of shaped graphene with mold 1 (400 nm in width and 100 nm in depth), and (h) shows the zoomed AFM profile. i) Raman spectra mapping of unstrained graphene and strained graphene in the nanotrench.

the help of molecular dynamics simulations to demonstrate the induced strain in graphene along the trench. The calculated strain profile is depicted in Figure 2b with largest strain located at the edge of the nanotrench. We also used variable-separation scanning tunneling microscopy (VS-STM) to examine the influence of the inhomogeneous local strain on the local electronic structure of the strained graphene sheet. We have selected seven points located at the curved graphene, as marked in Figure 2b. Point 1 is far away from the nanotrench, showing no strain at this point. The normalized differential conductance (dI/dV)–V is proportional to the surface density of states in graphene providing an estimate of the local effective bandgap. The normalized differential conductance (dI/dV)–V as a function of bias voltage is depicted in Figure 2c at designated locations as shown in Figure 2b which confirms the opening of the electronic bandgap in strained graphene. For the unstrained graphene above the trench (point 1), the linear steep slope indicates that this location is metallic suggesting that the bandgap is close to zero. However, at the edge of the trench (point 2), the negligible conductance in a large bias voltage region indicates

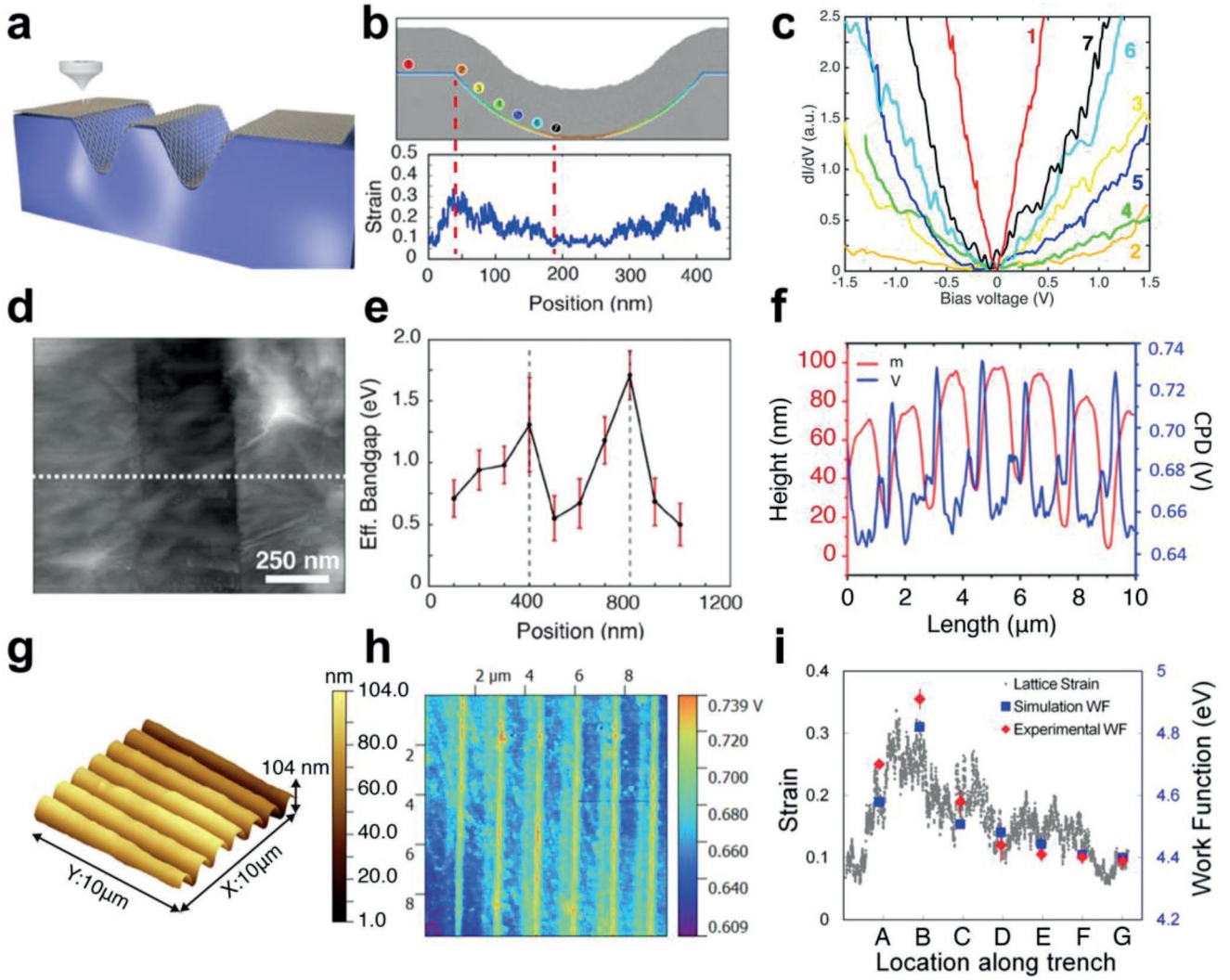

Figure 2. a) Schematic of the STM measurement on nanoimprinted graphene sheet. b) The calculated strain as a function of position along the trench using MD simulations, the inset shows the details of locations of bandgap measurements by STM (room temperature in constant-current mode, with I_{setp} = 0.2 nA and V_{bias} = 2 V). c) The representative (dI/dV)/I–V measurements on the patterned graphene sheet at various locations from point 1 to point 7, as shown in the inset of (b). d) Scanning tunneling microscopy image of graphene strained on the same nanotrench, and e) the corresponding effective bandgaps as a function of position along the white dashed line in (d). f) Profiles for topology and CPD. g) Atomic force microscopy (AFM) 3D surface profile of topology of graphene on silicon mold, and h) the corresponding KPFM image. i) DFT calculated and measured results of work function for the strained graphene at various locations along the trench.

a large strain induced bandgap opening. The bandgap opening decreases when the induced strain decreases at the respective position on the slope of the trench. Figure 2d depicts the STM figure of the strained graphene across the same nanotrench (with dimensions of 400 nm width and 100 nm depth). To better illustrate the bandgap opening of graphene, we have selected ten points along the same trench, and Figure 2e shows the corresponding effective bandgaps as a function of distance (nm) across the trench as shown by the dashed white horizontal line in Figure 2d. The dI/dV curves for selected points in Figure 2e are included in Figure S2 in the Supporting Information. The highest effective bandgaps of 1.3 ± 0.38 and 1.7 ± 0.24 eV are observed at the edge of the trench marked with the vertical dashed line whereas smaller bandgap openings ranging from 0.55 ± 0.14 and 1.15 ± 0.14 eV are observed in the interior region of the trench. Thus, we observed the opening of the bandgap of graphene up to 1.7 eV by straining in one step solely using laser shock produced large strains. The reason for the opening of the bandgap at the trench can be attributed to combined elastic and plastic strains, which will be discussed later. Recent studies about strain-induced graphene suggest that the bandgap opening is contributed from elastic in-plane straining.[38–40] On the other hand, this plastic–elastic strain can also tune Fermi level of graphene, leading to the elimination of energy barrier caused by misalignment of Fermi level in graphene–semiconductor heterojunction. Figure 2g shows the topology image of laser shock imprinted graphene sample on Si/SiO_2 mold, where the sample surface is uniformly and periodically imprinted. Figure 2f shows the CPD along the sample surface, ranging from 0.732 to 0.643 V. Profile of the graphene

sample and its corresponding KPFM is measured as shown in Figure 2h. Based on density functional theory calculation of the work functions of the plastic–elastic strained graphene, the work functions of graphene at seven locations from the edge of the trench to the center (points A–G) is observed to increase substantially with increase of strain, as shown in Figure 2i. The work function at the edge location of the trench with the largest strain was found to be a maximum (4.82 eV) and the work function at center was found to be a minimum (4.40 eV) from theoretical calculations. The measured work functions of the strained graphene trench at the corresponding seven locations in Figure 2b are found to be in the range of 4.39–4.91 eV, which are obtained by subtracting the CPD from the work function of the tip. Due to the measured work function results, the tunable Fermi level of graphene can be up to ≈0.6 eV, providing an important energy barrier self-alignment capability to achieve high performance for graphene–semiconductor devices.

Laser shock on another mold (mold 2) with 300 nm width and 100 nm depth was also carried out. The effective bandgap as a function of distance for mold 2 is illustrated in Figure S3 in the Supporting Information. When we compared the results for two different molds (mold 1 and mold 2), we observed a striking difference between bandgap plots, which implies that the edge region has bandgap opening as high as 2.1 ± 0.25 eV in mold 2 case. The central regions exhibit a small bandgap of 0.4 eV in the case of mold 1, whereas the bandgap is as high as 1.0 eV in the central region for the mold 2 case. This is due to larger strain in mold 2 with narrower width, which suggests that laser shock imprinting technique can modulate the levels of strain in graphene by substrate design to precisely tune its bandgap. **Figure 3**a displays the large-scale STM mapping of laser-shock-induced patterned graphene. The inset shows the fast Fourier transform (FFT) results for the graphene pattern, the periodicity of the signal indicates that the prominent bandgap opening coincides with the pattern and no break in larger scale graphene is induced by laser shock. Figure 3b shows the SEM image of the patterned graphene. Figure 3c–i illustrates the STM measured *I*–*V* curves at several locations along the yellow line on Figure 3a. With the laser-shock-induced strain decreasing, the *I*–*V* curve steepens, and when the strain increases, the *I*–*V* curve becomes flatter, indicating the periodic modulation of bandgap opening in graphene.

Figure 4a is a high-resolution TEM (HRTEM) image of the single-layer graphene strained by mold 1. A close-up view of the marked region is presented in Figure 4b, revealing aligned carbon atoms along three directions (orange arrows). Yellow hexagons marking carbon rings with alternate atoms are illustrated in Figure 4c. To evaluate the uniformity in the structure of graphene, the blue triangle is depicted in Figure 4e, in which three blue edges are identical with the orange arrows in Figure 4b. Figure 4d shows another region with a larger visible graphene structure. The close-up view of a marked region of Figure 4d is shown in Figure 4e along with the strain assessment measured by atomic distances. It is observed that atoms in two directions are relatively closer than the equilibrium distances in graphene as well as atomic distances in the third direction are larger, indicating nonuniform straining of graphene. We have also observed tension in one direction and compression in other direction, inducing shear strain and bond angle changes in graphene structure. The atomic distances from TEM images were used to assess strain and to validate the molecular dynamics simulation results. Omicron (UHV) STM system was used to obtain the atomic resolved topographic image (I = 10 nA, V = 0.2 V) and study the effect of laser shock straining on the atomic movements and reconfigurations. The STM images of graphene at three different locations along the trench which experienced different levels of straining are shown in Figure 4f–h. In Figure 4f near the trench valley, the hexagonal structure of graphene is preserved with only small distortion caused by atomic displacements, due to smallest strain in this area. However, at another location on the slope of trench (Figure 4g), higher distortion in the hexagonal structure as compared to Figure 4f can be observed, indicating higher levels of elastic strain in laser shocked graphene. At the trench edge location with the largest strain (Figure 4h), few Stone–Wales defects are observed to indicate the occurrence of plastic deformations. Such reconfigurations occur in atomic sheets to release the strain in the systems. High-resolution TEM cross sectional view (Figure S4, Supporting Information) was added to study the straining effects from the lattice parameters in the laser shock strained graphene on a 300 nm width trench mold. The pixel intensity profile (Figure S4a, Supporting Information) was used to calculate the lattice distance between neighboring atoms. The elastic lattice strain can be estimated by calculating the distance between second neighboring carbon atoms compared to that of the unstrained lattice parameters (0.243 nm) at six locations (Figure S4c, Supporting Information). The points of higher strains indicated plastic deformations, i.e., presence of Stone–Wales defects and the reference distances for second neighboring carbon atom distances for such 5-7-7-5 membered rings were taken from the simulation as depicted in Figure S4d in the Supporting Information. The strains at various positions were summarized in Figure S4b in the Supporting Information. Thus, we conclude that laser shock can result in designed strain profile in graphene sheet leading to extreme levels of straining which generate plastic strain-induced atomic reconfigurations in graphene such as Stone–Wales defect formation and vacancy formations. Based on the HRTEM, we have also observed distinct deformations in inhomogeneous straining multilayer graphene induced by laser shock, as shown in Figure S5 in the Supporting Information. Even though the multilayer sample may not be as technically promising as single-layer graphene, its ease of handling in practical devices makes it worth evaluating. In some designs the plastic strain induced at the edge of the trench is not desirable in graphene, since it creates huge distortions as compared to the unstrained graphene; however, it is acceptable under a tolerable level such that it would not disturb the atomic skeleton of graphene. To further prove the large bandgap opening in laser shock is also applicable to mechanical exfoliated graphene sample, we also measured photoluminescence (PL) spectrum of inhomogeneous straining graphene. From the results (Figure S6, Supporting Information), the peak near 675 nm is PL response from Au substrate, which exists in all measured results. The PL result of graphene at the edge (point 1) presents a distinct broad peak with the end at 800 nm, indicating the large bandgap opening due to the large elastoplastic strain. With the decrease of strain from the edge to the center (points 2–4), the reduction of PL intensity

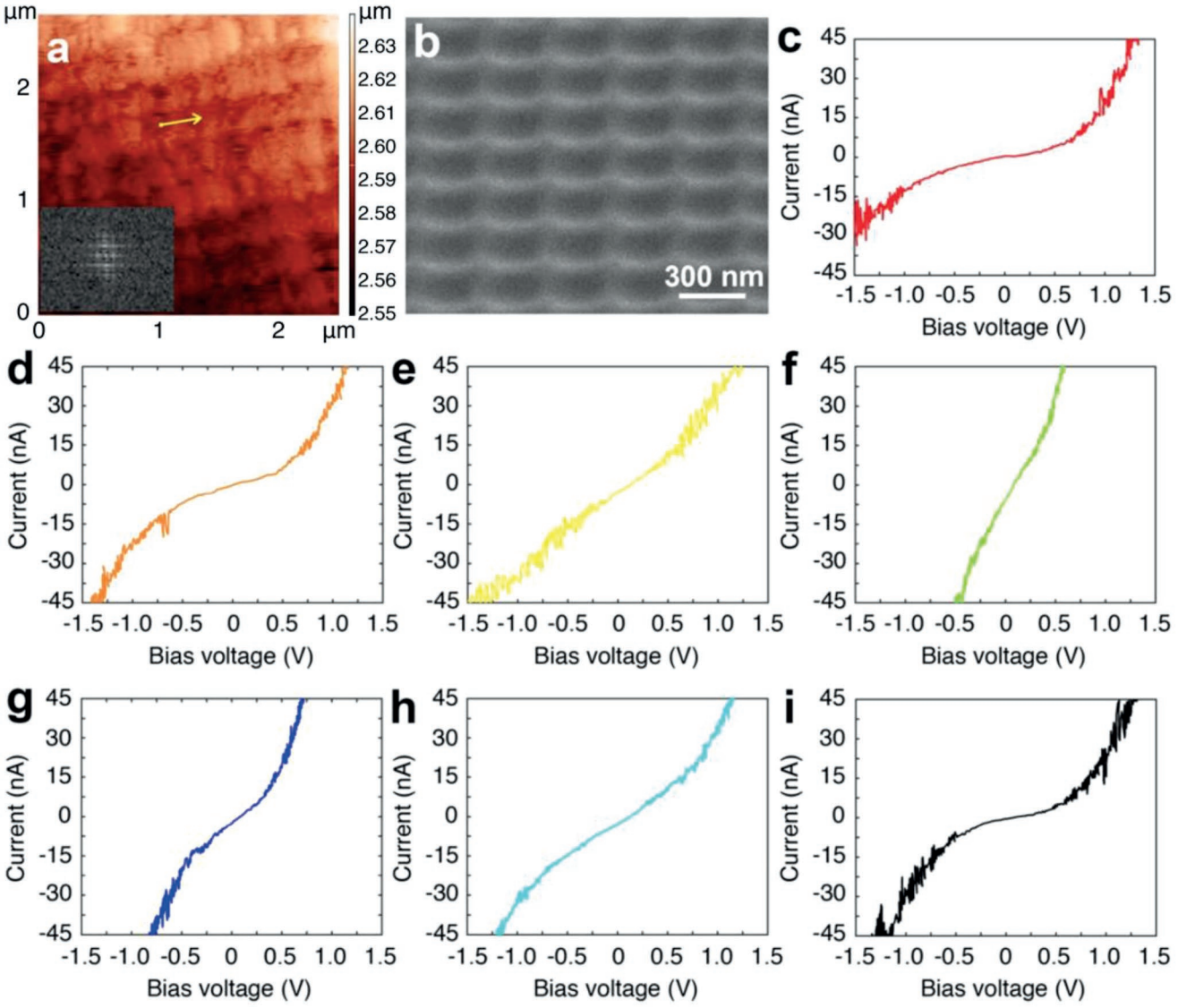

Figure 3. Large-scale patterned graphene sheet. a) STM mapping and b) SEM image of the patterned graphene. The inset in (a) shows the FFT results, which indicates the periodicity of patterned graphene. c–i) The STM current measured at several locations on the yellow line on (a), which indicates the periodic modulation of graphene's bandgap.

which is related with bandgap of graphene is observed, suggesting the reduction of bandgap opening with the decrease of laser-shocking-induced strain. The strong PL signal suggests that strained monolayer graphene possesses high quality. Thus, it would retain mobility which is perhaps the most significant attribute of graphene useful for fast nanoelectronic applications such as in FETs, sensing, THz wave guiding, etc.

For strained graphene, the crystal structure is observed to be skewed hexagonal shape, which is influenced by both axial and shear strain components. The bond angles of carbon atoms in graphene are also observed to be different than 120°, these results confirm asymmetric levels of inhomogeneous straining in graphene at the atomic scale. Since the enhanced level of strain differences in different directions would cause enormous asymmetries in the system, the dislocations in graphene would break the local symmetry thereby causing local rise of potential energy. We have closely followed experimental results on bandgap opening with molecular dynamics simulations of laser shock straining of graphene and then estimated bandgap employing DFT methods. It was not feasible to conduct simulations for the scale of the actual trench dimensions due to the enormous time and memory limitations; however, we kept the simulated depth-to-diameter ratio same as the real cases. Simulations were carried out on three different configurations to study the effect of the aspect ratio on straining and the bandgap opening of graphene. Further details of the molecular dynamics and DFT simulations are explained in the Supporting Information. To better validate the hypothesis that the bandgap opening was due to localized dislocation-induced plasticity and asymmetric elasticity, we have focused on the stress strains at three locations, namely A, D, and G, located at the edge of trench, slope of trench, and center of trench, respectively.

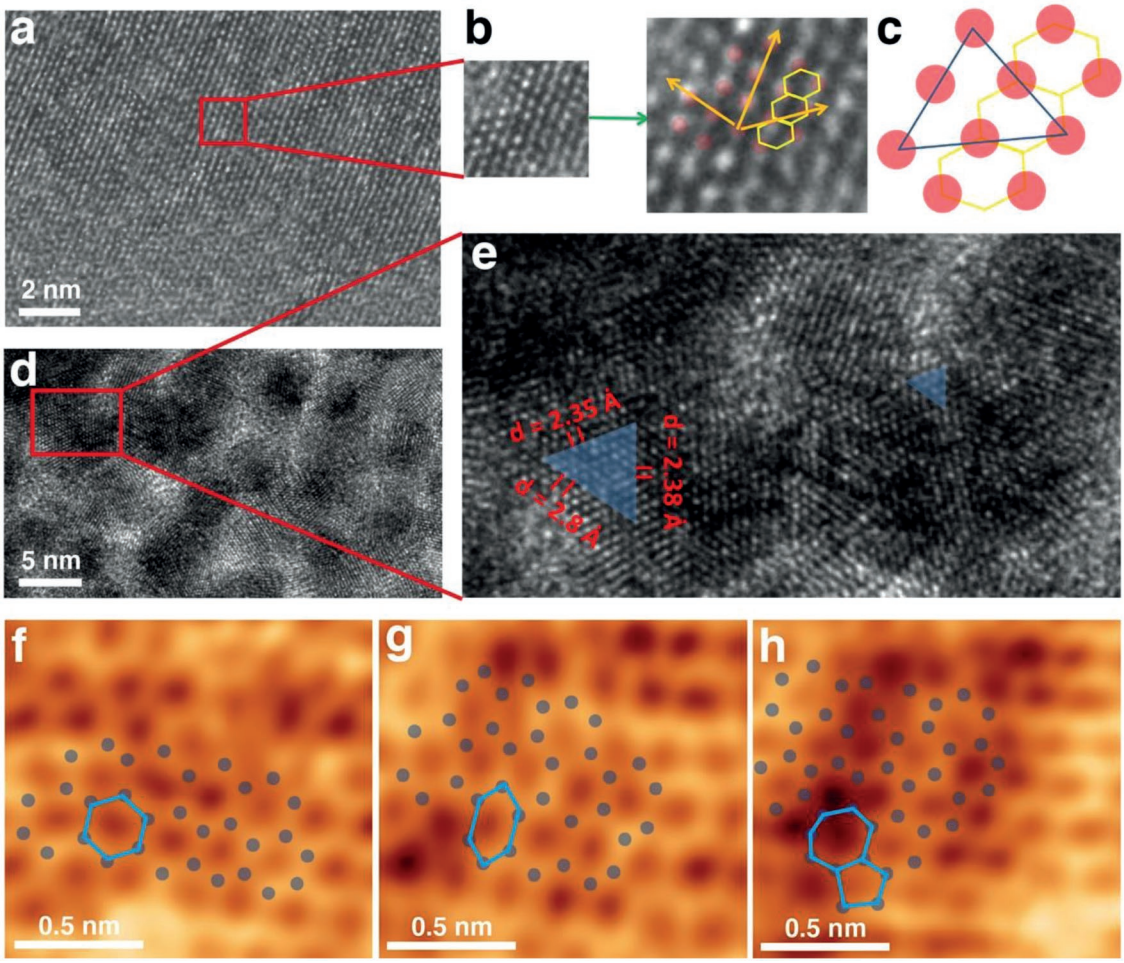

Figure 4. a) TEM image, b) HRTEM image of selected region shown in (a); c) atomic spacing in (b). d) TEM image of another region of strained graphene. e) HRTEM of the region shown in (d). Distances along three directions are shown in (e). Omicron (UHV) STM system was used to obtain the atomic resolved topographic image ($I = 10$ nA, $V = 0.2$ V) and study the effect of laser shock straining on the atomic movements and reconfigurations. f–h) STM images of strained graphene sheet at three different locations, from the trench valley, the slope of trench, and the trench edge, respectively. The atomic crystal structure is marked by light blue lines.

Permanent deformation was observed only at the edge for all three configurations which confirms that plasticity is observed only at the corner of strained graphene. Continuum crystal plasticity defines displacement field at every material point as against to atomistic description where we only have discrete atomic positions. Thus, to define a gradient, the displacement field is linearly interpolated between the atoms.[47] Stukowski and Arsenlis[48] developed a technique of separation of elastic and plastic decomposition of the deformation applied in molecular dynamics. With this technique, the bond vectors are mapped to the neighboring atoms to derive a stress-released state to measure atomic strains. More details of strain calculations are discussed in the Supporting Information.

The mechanical responses of the strained graphene and the atomic lattices for the configuration with depth-to-diameter ratio of 100 nm/400 nm are studied as depicted in **Figure 5**. Since Stone–Wales 5-7-7-5 defects in graphene represent evidence of plastic straining, the elastoplastic stress–strain response is observed only at location A (edge of nanotrench), as seen in Figure 5a, where graphene sustains largest strain. The plastic regime is found beyond strains of 0.18 for this configuration. The atomic model of the deformed configuration at location A is depicted in Figure 5b. Ratios of the bond lengths detected from simulations to the bond length of pristine graphene were calculated and plotted as seen in Figure 5b, where green marks average bond length of 1.42 Å. Onset of plasticity is marked by Stone–Wales 5-7-7-5 defects which are observed in Figure 5b. Extreme ratios are observed around plastically deformed 5-7-7-5 defects, leading to the modifications in the electronic properties of graphene. Thus, the large bandgap opening around location A is mainly due to plastic regime marked by Stone–Wales defects. Figure 5c reveals that the stress–strain behavior of graphene at location D (the trench slope) is purely elastic without any Stone–Wales 5-7-7-5 defects. However, as seen from Figure 5d, the different colors of these bonds represent the different relative bond lengths of graphene under the trench slope, displaying strongly asymmetric deformations in the form of six-membered rings. Interestingly, there were no plastic

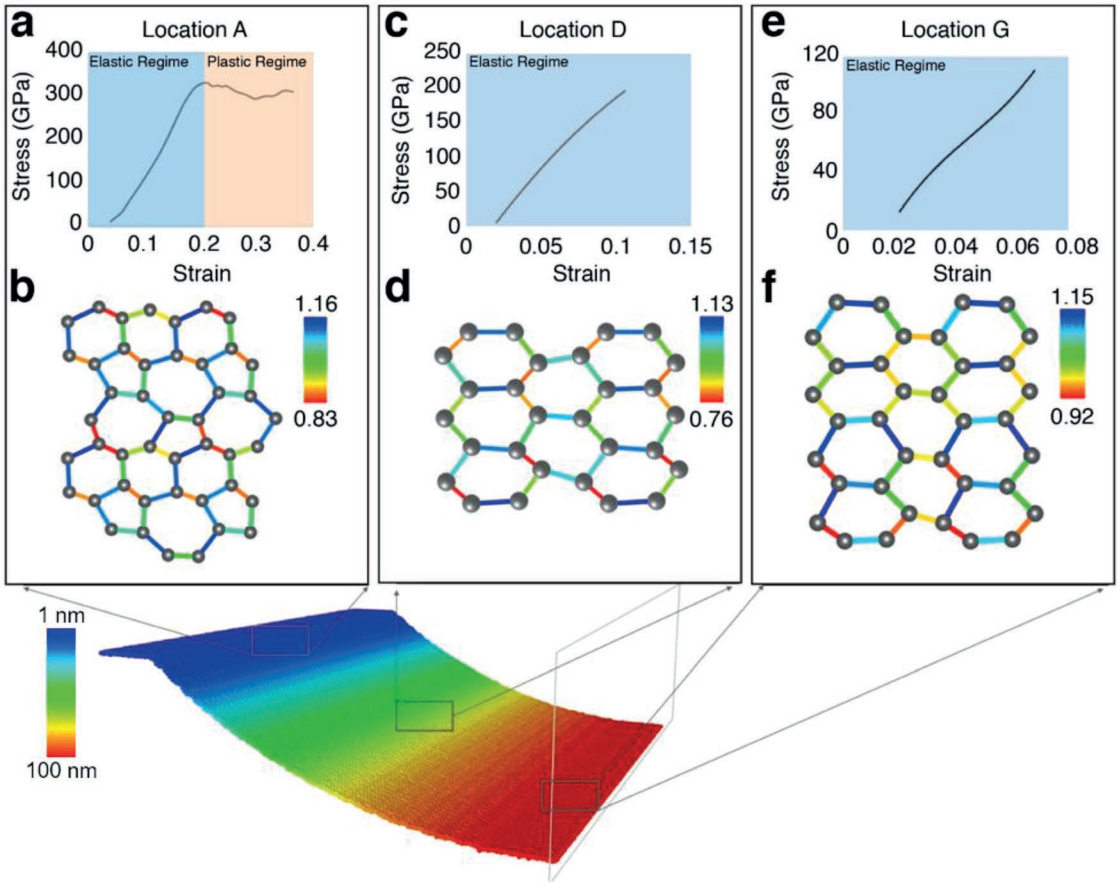

Figure 5. a) The stress–strain response extracted at the edge of the nanoshaped graphene. It is clear from the plot that graphene undergoes through elastoplastic deformation which is also depicted by the 5-7-7-5 defects seen from (b). Ratios of bond lengths were calculated and plotted as seen in (b) where green marks the average bond length of pristine graphene 1.42 Å. c,e) The elastic stress–strain response at location D and location G of deformed graphene and (d) and (e) denote bond length ratio. It is interesting to note that bandgap opening of 0.527 eV was observed at this location due to asymmetric strains because of asymmetric bond length ratios even in elastic regime.

strains at location D (center of trench), yet a bandgap opening of up to 0.87 eV was observed at this location due to asymmetric elastic straining. In Figure 5e, the stress–strain behavior at location G is also elastic but relatively less as compared to location D. This relatively elastic deformation leads to more moderate asymmetric bond lengths in graphene six-membered ring (Figure 5f), meaning the narrowest bandgap opening. The evolutions of atomic structure at three locations A, D, and G of strained graphene can also be revealed through molecular dynamics simulation, as shown in Figures S7–S9, dynamically verifying the different deformation process of atomic structure evolution in graphene under different strain. The description of the dynamic processes of molecular structure at locations A, D, and G are demonstrated by MD simulation as shown in Video S2 in the Supporting Information.

We have closely followed experimental results on bandgap opening DFT simulations, to estimate the bandgaps in inhomogeneous straining graphene opened under different depth-to-diameter ratios, as shown in **Figure 6**. The bandgap values calculated by DFT vary based on location across the nanotrench depending on the level of straining. These values are often underestimated by DFT calculations as reported by previous researchers.[9] For the model of depth-to-diameter ratio of 100 nm/400 nm, the effective bandgaps show a gradually decreasing trend from points A–G. It is interesting to note that band opening of up to 0.527 eV is observed at location G due to asymmetric strains in elastic regime, whereas band opening of ≈1.365 eV is observed near the edge of the nanotrench (A point) due to dislocation-induced plasticity. The other two models of graphene (with depth-to-diameter ratios of 100 nm/300 nm and 100 nm/500 nm, details in Figures S12 and S13, Supporting Information) are also investigated to indicate the higher strains in 3D inhomogeneous straining graphene with higher depth-to-diameter ratio, implying larger bandgap opening under higher depth-to-diameter ratio. The bandgap opening is observed to be higher at the edge of the trench as compared to the center of the trench, attributing to the stronger sublattice asymmetry break of graphene at the edge of the trench. It is important to note that if the depth-to-diameter ratio is increased steeply (over 50%), then the graphene lattice at the edge of the trench could break and graphene would be converted to amorphous form.

Laser-shock-modulated inhomogeneous straining is thus an outstanding optomechanical technique with immense potential

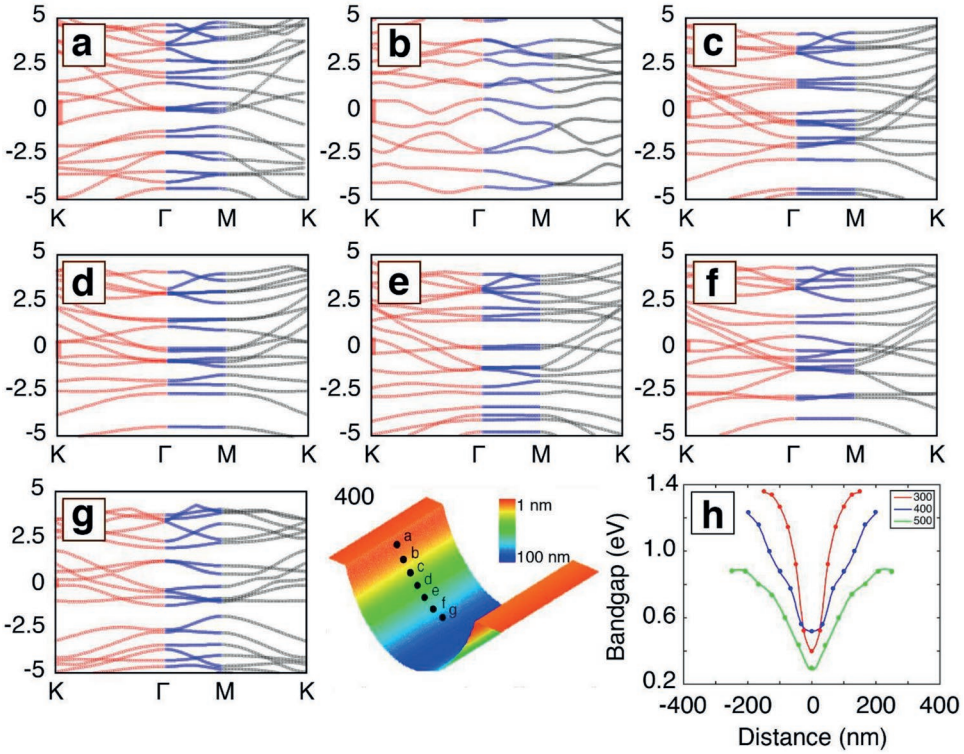

Figure 6. Band structure for strained graphene at different locations marked (a–g) from edge to center were plotted. The bandgap opening at regions near the edge were found out due to onset of plasticity, and the bandgap opening near the center was found out due to asymmetric elastic straining in graphene. h) The bandgaps at different locations from edge to center for all three configurations with diameters of 300 nm (aspect ratio: 33%), 400 nm (aspect ratio: 25%), and 500 nm (aspect ratio: 20%). Higher bandgap opening is observed at lower aspect ratios near edge of strained graphene.

for applications, which would create semiconductor zones at the shallow slanted portions of strained graphene. The shape of graphene is at nanoscale from 30 to 200 nm, which can be controlled through precise design of the nanomold. A desired bandgap can be provided by designing the mold dimension and applying appropriate laser shock pressure. This opens new possibilities for novel applications based on complicated nanostructures in 2D materials, such as topological insulators and quantum pseudo-magnetic field. Such freedom of designing the level of electronic bandgap and the feasibility of selection of such high bandgap zones at desired locations can also yield a new class of graphene-based metamaterials and can have a huge impact on future generations of optical and optoelectronic devices.

In summary, laser shock nanostraining of graphene on e-beam fabricated nanotrench-shaped nanomolds has been evaluated for electronic bandgap engineering by scanning tunneling spectroscopy and other analytical techniques. For the first time, strain tunable bandgap creation is observed in graphene with the bandgap value up to 1.7–2.1 eV which attributes to asymmetric elastic–plastic straining behavior under the nanoscale ultrahigh strain rate imprinting process during laser shocking. Such a high level of bandgap development in graphene without any extrinsic effects beyond graphene itself has not been reported earlier and is first of its kind. Numerous applications in electronics and optoelectronics based on such tunable bandgap formation in graphene are enabled by this capability of converting the semimetallic graphene to semiconducting graphene with designed bandgaps.

Experimental Section

3D Straining of Graphene: CVD graphene coated on copper sheet was first transferred on SiO_2 mold by wet chemical transfer method. In brief, methyl methacrylate was coated (100 nm) onto graphene and then it was hardened to poly(methyl methacrylate) (PMMA) by heating the sample at 60 °C for 30 min. Copper was then etched away by using aqueous $FeCl_3$ solution. The copper-free sample was then gently transferred to clean deionized water and it was then transferred to fresh water for 3–4 times until there was no yellowish color remaining in water even after the sample was kept for 30 min. The graphene sheet having PMMA on the top was then transferred to the SiO_2 mold while it was floating on the water surface. PMMA was then removed by dissolving it in acetone followed by isopropyl alcohol and deionized water, respectively. The sample was then adequately dried in N_2 jet. The dried graphene was laser shock nanostrained by employing laser shock pressure on graphene sheet stretched on the SiO_2 mold. A pulsed (10 ns) Q-switch Nd:YAG laser (Continuum Surelite III, Wavelength: 1064 nm) was used as an energy source for ablation. The laser beam diameter of 4 mm was attained by a focusing lens, which was calibrated by a photosensitive paper (Kodak Linagraph, type: 1895). Glass slide was used as the confining media, and aerosol graphite painting (Asbury Carbons, USA) was coated on thin (4 μm) aluminum foil (Lebow Company Inc., Bellevue, WA, USA) as the ablative layer. Laser scanning was enabled by placing the sample on an X–Y–Z computer-controlled motorized stage. Silicon dioxide molds with nanofeatures were fabricated through electron beam lithography or focused ion beam (FIB) milling and the trench width was 400 and 300 nm

for the two trenches (mold 1 and mold 2). Depth was 100 nm for both mold trenches. To press the whole sample into the trenches, multiple laser pulses were implemented, the laser shocking location for each pulse was controlled by the X–Y–Z motorized stage.

Microscopy: The surface morphology was imaged by SEM (Hitachi S-4800 field-emission scanning electron microscope) at an operating voltage of 5 kV and an atomic force microscope (Veeco Dimension 3100 AFM) was employed to scan the nanoimprinted graphene surface at nanoscale under tapping mode.

STM, VS-STM, and KPFM: An omicron ultrahigh vacuum (UHV) STM system was used to obtain the atomic resolved topographic image (I = 10 nA, V = 0.2 V). Scanning tunneling microscopy was then performed at room temperature. STM was performed at room temperature in constant-current mode, with a set-point current between 200 and 350 pA and an applied sample bias between 2 and 3 V. The differential conductance, dI/dV, was measured using VS-STM, in which both the bias voltage and tip-sample separation were varied in a controlled manner. The dI/dV measurements were conducted at room temperature using a lock-in technique with a modulation voltage of frequency 1 kHz and amplitude 100 mV. A monolayer graphene was transferred onto the Al foil, followed by laser shock imprinting (LSI) process toward a 1600 nm periodicity trench mold. Kelvin probe force microscopy (KPFM) was used to characterize both topology and the distribution of contact potential difference (CPD) along the laser shocking imprinted area.

PL Measurements: Photoluminescence was measured by using Alpha 300R confocal Raman imaging system (WITec) at room temperature. The graphene was transferred onto the SiO_2/Si nanomold, and then Au electrode was deposited, followed by laser shock processing to compress the graphene into the nanonold. PL measurement was conducted before the electrical property testing (see Figure S4 inset in the Supporting Information for the structure of the device).

TEM: The TEM samples for strained graphene were prepared by lift-out method by FEI Nova 200 focused ion beam with a Klöcke nanomanipulator, to cut cross sectional view of the graphene vertical to the nanotrench. The top view of graphene near the edge of the nanotrench was also obtained for TEM by FIB. The microstructures were examined using an FEI Titan 80-300 and a Tecnal T20 transmission electron microscope.

Simulation: Molecular dynamics simulations had been conducted to gain an insight of the deformation of the monolayer graphene and to understand the effect of the aspect ratio on the straining levels in graphene. Tight binding density functional theory had been employed to calculate the band structure of the strained graphene as a function of position for 3 molds with different aspect ratios. Work function at different seven locations on the strained graphene had also been calculated using DFT calculations. Details of calculation are described in the Supporting Information.

Supporting Information

Supporting Information is available from the Wiley Online Library or from the author.

Acknowledgements

Financial assistance in the form of National Research Council Senior Research Associateship (G.J.C.), and NSF Grant Nos. CMMI-0547636 and CMMI 0928752 (G.J.C.) had been crucial for these experiments. National Natural Science Foundation of China (Grant No. 61704061). P.K. acknowledges financial support from Science and Engineering Research Board, Dept. of Sci. and Tech., Govt. of India in the form of The Ramanujan Fellowship (Sanction No. SB/S2/RJN-205/2014).

Conflict of Interest

The authors declare no conflict of interest.

Keywords

bandgap engineering, optomechanical 3D straining, single-layer graphene

Received: January 24, 2019
Revised: February 19, 2019
Published online: March 29, 2019

[1] K. S. Novoselov, A. K. Geim, S. V. Morozov, D. Jiang, Y. Zhang, S. V. Dubonos, I. V. Grigorieva, A. A. Firsov, *Science* **2004**, *306*, 666.
[2] K. S. Novoselov, A. K. Geim, S. V. Morozov, D. Jiang, M. I. Katsnelson, I. V. Grigorieva, S. V. Dubonos, A. A. Firsov, *Nature* **2005**, *438*, 197.
[3] A. K. Geim, K. S. Novoselov, *Nat. Mater.* **2007**, *6*, 183.
[4] F. Schwierz, *Nat. Nanotechnol.* **2010**, *5*, 487.
[5] S. Bae, H. Kim, Y. Lee, X. Xu, J.-S. Park, Y. Zheng, J. Balakrishnan, T. Lei, H. Ri Kim, Y. I. Song, Y.-J. Kim, K. S. Kim, B. Özyilmaz, J.-H. Ahn, B. H. Hong, S. Iijima, *Nat. Nanotechnol.* **2010**, *5*, 574.
[6] T.-H. Han, Y. Lee, M.-R. Choi, S.-H. Woo, S.-H. Bae, B. H. Hong, J.-H. Ahn, T.-W. Lee, *Nat. Photonics* **2012**, *6*, 105.
[7] X. Li, H. Zhu, K. Wang, A. Cao, J. Wei, C. Li, Y. Jia, Z. Li, X. Li, D. Wu, *Adv. Mater.* **2010**, *22*, 2743.
[8] F. Schedin, A. K. Geim, S. V. Morozov, E. W. Hill, P. Blake, M. I. Katsnelson, K. S. Novoselov, *Nat. Mater.* **2007**, *6*, 652.
[9] J. T. Robinson, F. Perkins, E. S. Snow, Z. Wei, P. E. Sheehan, *Nano Lett.* **2008**, *8*, 3137.
[10] C.-H. Lu, H.-H. Yang, C.-L. Zhu, X. Chen, G.-N. Chen, *Angew. Chem.* **2009**, *121*, 4879.
[11] A. N. Grigorenko, M. Polini, K. S. Novoselov, *Nat. Photonics* **2012**, *6*, 749.
[12] J. Chen, M. Badioli, P. Alonso-González, S. Thongrattanasiri, F. Huth, J. Osmond, M. Spasenović, A. Centeno, A. Pesquera, P. Godignon, A. Zurutuza Elorza, N. Camara, F. de Abajo, R. Hillenbrand, F. H. L. Koppens, *Nature* **2012**, *487*, 77.
[13] K. J. Tielrooij, J. C. W. Song, S. A. Jensen, A. Centeno, A. Pesquera, A. Zurutuza Elorza, M. Bonn, L. S. Levitov, F. H. L. Koppens, *Nat. Phys.* **2013**, *9*, 248.
[14] D. Sun, G. Aivazian, A. M. Jones, J. S. Ross, W. Yao, D. Cobden, X. Xu, *Nat. Nanotechnol.* **2012**, *7*, 114.
[15] C. Zeng, E. B. Song, M. Wang, S. Lee, C. M. Torres, J. Tang, B. H. Weiller, K. L. Wang, *Nano Lett.* **2013**, *13*, 2370.
[16] F. Xia, T. Mueller, Y.-M. Lin, A. Valdes-Garcia, P. Avouris, *Nat. Nanotechnol.* **2009**, *4*, 839.
[17] A. K. Geim, *Science* **2009**, *324*, 1530.
[18] K. S. Novoselov, V. I. Fal'ko, L. Colombo, P. R. Gellert, M. G. Schwab, K. Kim, *Nature* **2012**, *490*, 192.
[19] S.-H. Lee, H.-J. Chung, J. Heo, H. Yang, J. Shin, U.-I. Chung, S. Seo, *ACS Nano* **2011**, *5*, 2964.
[20] V. M. Pereira, A. H. Castro Neto, *Phys. Rev. Lett.* **2009**, *103*, 046801.
[21] G. W. Jones, V. M. Pereira, *New J. Phys.* **2014**, *16*, 093044.
[22] L. S. Panchakarla, K. S. Subrahmanyam, S. K. Saha, A. Govindaraj, H. R. Krishnamurthy, U. V. Waghmare, C. N. R. Rao, *Adv. Mater.* **2009**, *21*, 4726.
[23] B. Guo, Q. Liu, E. Chen, H. Zhu, L. Fang, J. R. Gong, *Nano Lett.* **2010**, *10*, 4975.
[24] R. Balog, B. Jørgensen, L. Nilsson, M. Andersen, E. Rienks, M. Bianchi, M. Fanetti, E. Lægsgaard, A. Baraldi, S. Lizzit,

Z. Sljivancanin, F. Besenbacher, B. Hammer, T. G. Pedersen, P. Hofmann, L. Hornekær, *Nat. Mater.* **2010**, *9*, 315.
[25] D. V. Kosynkin, A. L. Higginbotham, A. Sinitskii, J. R. Lomeda, A. Dimiev, B. Price, J. M. Tour, *Nature* **2009**, *458*, 872.
[26] P. Kumar, L. S. Panchakarla, C. N. R. Rao, *Nanoscale* **2011**, *3*, 2127.
[27] S. Y. Zhou, G.-H. Gweon, A. V. Fedorov, P. N. First, W. A. de Heer, D.-H. Lee, F. Guinea, A. H. Castro Neto, A. Lanzara, *Nat. Mater.* **2007**, *6*, 770.
[28] F. Guinea, M. I. Katsnelson, A. K. Geim, *Nat. Phys.* **2010**, *6*, 30.
[29] Z. H. Ni, T. Yu, Y. H. Lu, Y. Y. Wang, Y. P. Feng, Z. X. Shen, *ACS Nano* **2008**, *2*, 2301.
[30] T. M. G. Mohiuddin, A. Lombardo, R. R. Nair, A. Bonetti, G. Savini, R. Jalil, N. Bonini, D. M. Basko, C. Galiotis, N. Marzari, K. S. Novoselov, A. K. Geim, A. C. Ferrari, *Phys. Rev. B* **2009**, *79*, 205433.
[31] N. Rosenkranz, M. Mohr, C. Thomsen, *Ann. Phys.* **2011**, *523*, 137.
[32] S.-M. Choi, S.-H. Jhi, Y.-W. Son, *Phys. Rev. B* **2010**, *81*, 081407R.
[33] S.-M. Choi, S.-H. Jhi, Y.-W. Son, *Nano Lett.* **2010**, *10*, 3486.
[34] G. Gui, J. Li, J. Zhong, *Phys. Rev. B* **2008**, *78*, 075435.
[35] G. Cocco, E. Cadelano, L. Colombo, *Phys. Rev. B* **2010**, *81*, 241412R.
[36] J. Hicks, A. Tejeda, A. Taleb-Ibrahimi, M. S. Nevius, F. Wang, K. Shepperd, J. Palmer, F. Bertran, P. Le Fèvre, J. Kunc, W. A. de Heer, C. Berger, E. H. Conrad, *Nat. Phys.* **2013**, *9*, 49.
[37] M. P. Ariza, R. Serrano, J. P. Mendez, M. Ortiz, *Philos. Mag.* **2012**, *92*, 2004.
[38] W. Yan, W.-Y. He, Z.-D. Chu, M. Liu, L. Meng, R.-F. Dou, Y. Zhang, Z. Liu, J.-C. Nie, L. He, *Nat. Commun.* **2013**, *4*, 2159.
[39] N. Levy, S. A. Burke, K. L. Meaker, M. Panlasigui, A. Zettl, F. Guinea, A. H. C. Neto, M. F. Crommie, *Science* **2010**, *329*, 544.
[40] N. N. Klimov, S. Jung, S. Zhu, T. Li, C. A. Wright, S. D. Solares, D. B. Newell, N. B. Zhitenev, J. A. Stroscio, *Science* **2012**, *336*, 1557.
[41] H. Gao, Y. Hu, Y. Xuan, J. Li, Y. Yang, R. V. Martinez, C. Li, J. Luo, M. Qi, G. J. Cheng, *Science* **2014**, *346*, 1352.
[42] T. Zhang, H. Gao, *J. Appl. Mech.* **2015**, *82*, 051001.
[43] X. Wang, L. Huang, Y. Peng, N. Huo, K. Wu, C. Xia, Z. Wei, S. Tongay, J. Li, *Nano Res.* **2016**, *9*, 507.
[44] Z. Wei, T. Hansen, M. Santella, X. Wang, C. R. Parker, X. Jiang, T. Li, M. Glyvradal, K. Jennum, E. Glibstrup, N. Bovet, X. Wang, W. Hu, G. C. Solomon, M. B. Nielsen, X. Qiu, T. Bjørnholm, K. Nørgaard, B. W. Laursen, *Adv. Funct. Mater.* **2015**, *25*, 1700.
[45] Q. H. Wang, K. Kalantar-Zadeh, A. Kis, J. N. Coleman, M. S. Strano, *Nat. Nanotechnol.* **2012**, *7*, 699.
[46] L. Ye, P. Wang, W. Luo, F. Gong, L. Liao, T. Liu, L. Tong, J. Zang, J. Xu, W. Hu, *Nano Energy* **2017**, *37*, 53.
[47] P. H. Mott, A. S. Argon, U. W. Suter, *Philos. Mag. A* **1993**, *67*, 931.
[48] A. Stukowski, A. Arsenlis, *Modell. Simul. Mater. Sci. Eng.* **2012**, *20*, 035012.